

---

This manuscript is a preprint and has been submitted for publication to JGR: Planets. Please note that, the manuscript is currently undergoing peer-review, but the manuscript has yet to be formally accepted for publication. Subsequent versions of this manuscript may have slightly different content. If accepted, the final version of this manuscript will be available via the ‘Peer-reviewed Publication DOI’ link on the right-hand side of this webpage. Please feel free to contact any of the authors; we welcome feedback.

---

1 **Lithology, pore-filling media, and pore closure depth**  
2 **beneath InSight on Mars inferred from shear wave**  
3 **velocities**

4 **Richard Kilburn<sup>1</sup>, Jhardel Dasent<sup>1</sup>, Vashan Wright<sup>1</sup>, and Michael Manga<sup>2</sup>**

5 <sup>1</sup>University of California San Diego, Scripps Institution of Oceanography, La Jolla, CA, 92037

6 <sup>2</sup>University of California Berkeley, Department of Earth and Planetary Science, Berkeley, CA, 94720

7 **Key Points:**

- 8 • Mars' upper crust (0-8 km) beneath InSight comprises fractured gas-filled rocks  
9 and weakly cemented sediments  
10 • Mars' deeper crust (8-20 km) beneath InSight could comprise fractured basalts  
11 or more-felsic igneous rocks with 0-23% porosity  
12 • No seismically detectable cryosphere exists in the crust and pores in the deeper  
13 crust host gas, liquid water, or up to 2% cement

---

Corresponding author: Richard Kilburn, [rkilburn@ucsd.edu](mailto:rkilburn@ucsd.edu)

## 14 Abstract

15 We quantify the volume and distribution of water, cement, sediments, and fractured  
 16 rocks within the Martian crust beneath NASA’s InSight (Interior Exploration using Seis-  
 17 mic Investigations, Geodesy, and Heat Transport mission) lander by using rock physics  
 18 models to interpret shear wave velocities ( $V_s$ ) measured from InSight data. The mod-  
 19 els assume that Mars’ crust comprises sediments and fractured rocks whose pores and  
 20 fractures host variable combinations of gas, liquid water, and mineral cements. Measured  
 21  $V_s$  in the upper crust (0-8 km) can be explained by layers of minimally (< 2%) cemented  
 22 sediments and gas-filled fractured basalts. Measured  $V_s$  in the deeper crust (8-20 km)  
 23 can be explained by fractured basalts or more felsic igneous rocks (modeled here as 100%  
 24 plagioclase feldspar) that is unfractured or has up to 23% porosity. Open pores in the  
 25 deeper crust could host gas, liquid water, and up to 2% cement. Modeled  $V_s$  are too low  
 26 for a seismically detectable ice-saturated cryosphere in the upper crust and temperatures  
 27 are too high to freeze liquid water in the deeper crust. Notably, with  $V_s$  alone, we are  
 28 unable to distinguish between liquid water and gas within the pores.

## 29 Plain Language Summary

30 Liquid water may have existed on Mars as oceans, rivers, or ground water. Sur-  
 31 face water was likely lost to space, buried as liquid water and ice, and/or incorporated  
 32 in subsurface minerals and mineral cements. The InSight lander on Mars has a seismome-  
 33 ter whose measurements can be used to estimate the velocity of seismic shear waves. Seis-  
 34 mic velocities change based on rock type and the material that fills the pores within rocks  
 35 (e.g., liquid water, gas, or ice and other mineral cements). We show that the measured  
 36 seismic velocities in the upper (0-8 km) crust can be explained by layers of gas-filled basalts  
 37 and minimally (2%) cemented sediments rather than ice-filled sediment or basalt. Mea-  
 38 sured seismic velocities in the deeper (8-20 km) crust can be explained by fractured basalt.  
 39 More feldspar-rich rocks could explain the velocities in the deeper crust and they could  
 40 be unfractured or have up to 23% porosity. Fractures within the deeper crust could host  
 41 liquid water, gas, and up to a couple percent of mineral cements.

## 42 1 Introduction

43 Quantifying the volume and distribution of Mars’ subsurface lithologies, mineral  
 44 cements, and liquid water are critical to unraveling the planet’s geologic evolution (Carr  
 45 & Head, 2003; Di Achille & Hynek, 2010; Carr & Head, 2019; Scheller et al., 2021). Mars’  
 46 crust comprises igneous and sedimentary rocks that are lithified and fractured to vary-  
 47 ing degrees (Tanaka et al., 2014; Golombek et al., 2018; Pan et al., 2020). Two open ques-  
 48 tions are (1) what is the depth where pores close entirely within the Martian crust and  
 49 (2) what percentages of existing pores host water as liquid or ice, or that was incorpo-  
 50 rated into other mineral cements.

51 Gravity and heat flow models provide constraints on Mars’ subsurface porosity and  
 52 pore closure depth (Clifford, 1993; Clifford et al., 2010; Goossens et al., 2017; Gyalay et  
 53 al., 2020; Wiczeorek et al., 2022). Goossens et al. (2017) used gravity data to infer that  
 54 Mars’ average bulk density in the upper 20 km is  $2,582 \pm 209$  kg/m<sup>3</sup>. From this bulk den-  
 55 sity, a porosity of 0.10 to 0.23 in the upper 20 km can be obtained. Wiczeorek et al. (2022)  
 56 later integrated gravity and shear wave velocity data to hypothesize that a lower den-  
 57 sity (higher porosity) layer extends to 8-11 or 20-23 km below the surface and the pores  
 58 close entirely beneath one of these depths. Gyalay et al. (2020) used heat flow models  
 59 to argue that pore collapse via thermally-activated viscous creep should occur between  
 60 12 km and 23 km below the surface. The transition from open to closed pores should  
 61 occur over 1 km (Gyalay et al., 2020). Gyalay et al. (2020)’s and Wiczeorek et al. (2022)’s

62 proposed pore closure depth overlaps with two possible seismic discontinuities ( $8\pm 3$  and  
63  $20\pm 5$  km) (Figure 1).

64 Surface exposures alongside heat and fluid flow models provide constraints on the  
65 presence, volume, and distribution of water within the Martian crust. Rover and satel-  
66 lite images showing sediment structures and stratigraphy characteristic of ancient delta,  
67 marine, and fluvial depositional environments alongside direct and remotely inferred ob-  
68 servations of ice and liquid water at the polar regions evidence past and current water  
69 on Mars (Carr, 1987; Baker, 2006; Orosei et al., 2018; Nazari-Sharabian et al., 2020). Ev-  
70 idence for past subsurface liquid water also includes Hesperian and Amazonian-aged out-  
71 flow channels, whose discharges were sometimes a few orders of magnitude greater than  
72 Earth’s largest floods (Colaprete & Jakosky, 1998; Carr & Head, 2002; Burr et al., 2002;  
73 Manga, 2004; Bibring et al., 2005; Clifford et al., 2010; Di Achille & Hynek, 2010; Ro-  
74 driguez et al., 2015; Weiss & Head, 2017; Voigt & Hamilton, 2018). Mars’ past surface  
75 water in rivers, lakes, and possible oceans may have been lost to space or infiltrated the  
76 ground (Colaprete & Jakosky, 1998; Bibring et al., 2005; Di Achille & Hynek, 2010). Liq-  
77 uid water may have percolated through the pores of rock layers, whose permeability may  
78 have been increased by impacts (Clifford, 1997; Wang et al., 2005). Heat flow models  
79 suggest that a 0-9 km and 10-22 km thick regional cryosphere could exist at Mars’ equa-  
80 tor and poles, respectively (Clifford et al., 2010). Atmospheric carbon dioxide may have  
81 dissolved in water, then precipitated as carbonate cement (up to 2%) (Boynnton et al.,  
82 2009; Halevy & Schrag, 2009; Adam et al., 2013). Thus, mapping Mars’ subsurface ice  
83 and other mineral cements, liquid water, and lithology may help constrain (1) the vol-  
84 ume of water buried versus lost to space (Jakosky, 2021), (2) the planet’s water budget  
85 and cycle through time (Clifford & Parker, 2001), (3) the fates of past surface water (Citron  
86 et al., 2018), (4) the volume of water sequestered by minerals, and (5) the lithology of  
87 Martian subsurface layers in the past and present (Mustard, 2019; Scheller et al., 2021;  
88 Wernicke & Jakosky, 2021).

89 Rock physics models and shear wave velocities  $V_s$  derived from seismograms col-  
90 lected by the seismometer on the InSight (Interior Exploration using Seismic Investiga-  
91 tions, Geodesy, and Heat Transport mission) lander provide opportunities to explore Mars’  
92 subsurface mechanical properties further.  $V_s$  is sensitive to several rock and sediment  
93 properties, including mineralogy, fracture density, porosity, and ice and other mineral  
94 cements (Mindlin, 2021; Dvorkin & Nur, 1996; Jenkins et al., 2005; Waite et al., 2009).  
95 The Martian crust beneath InSight has at least two seismically detectable km-scale lay-  
96 ers (Knapmeyer-Endrun et al., 2021).  $V_s$  are 1.7-2.1 km/s in the upper crust (i.e., be-  
97 tween 0 km and  $\sim 8$ -11 km) and 2-3.4 km/s in the deeper crust (i.e., between  $\sim 8$ -11 km  
98 and 20 km) (Figure 1). Interpretations using self-consistent fractured-media rock physics  
99 models (Te Wu, 1966; Berryman, 1980) indicate that  $V_s$  within the upper 8-11 km is lower  
100 than expected for a cryosphere (Manga & Wright, 2021; Wright et al., 2022).  $V_s$  between  
101 11 km and 20 km may be consistent with basalts whose fractures are 1-5% filled with  
102 calcite cement (Manga & Wright, 2021). Thus, Mars’ subsurface is likely a mix of sed-  
103 iments (i.e., layers with unconsolidated grains) and fractured layers of consolidated sed-  
104 iments or igneous rocks.

105 Our study uses granular and self-consistent fractured-media rock physics models  
106 to infer the volume and distribution of liquid water, ice and other mineral cements, and  
107 lithology from InSight-measured  $V_s$ . We infer that (1) the upper crust beneath InSight  
108 comprises layers of fractured gas-filled basalts and weakly cemented sediments, (2) the  
109 deeper crust could be fractured basalts or more felsic igneous rocks that are either un-  
110 fractured or has up to 23% porosity, (3) the pores of fractured rocks in the deeper crust  
111 could host liquid water, gas, or 2% cement and 98% liquid water or gas, and (4) no seis-  
112 mically detected ice-saturated cryosphere layer exists beneath InSight.

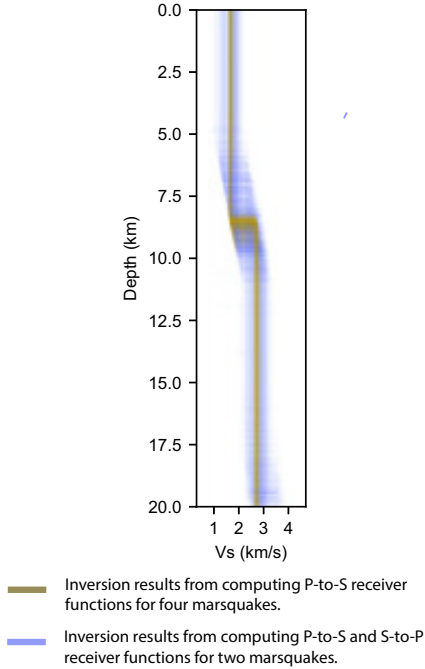


**Figure 1.** InSight derived shear-wave velocities ( $V_s$ ) (Knapmeyer-Endrun et al., 2021). The brown and purple lines show  $V_s$  from P-to-S receiver function analyses for four and two marsquakes, respectively.

## 2 Methods

We compare modeled and measured  $V_s$  to infer Mars’ subsurface mechanical properties, constraining model uncertainties with Monte Carlo simulations and sensitivity analyses. We use granular and fractured-media rock physics models to model  $V_s$  in the upper crust; we use only the fractured-media models for the deeper crust because we do not expect sediment layers in the deeper crust.

We calculate  $V_s$  from

$$V_s = \sqrt{\frac{\mu_e}{\rho}}, \quad (1)$$

where  $\mu_e$  and  $\rho$  are the effective shear modulus and bulk density, respectively. Rock physics models, described next, provide estimates for  $\mu_e$ . We estimate bulk density  $\rho$  using

$$\rho = \sum_i \phi_i \rho_i \quad (2)$$

where  $\rho_i$  and  $\phi_i$  are densities and volume fractions of the  $i^{\text{th}}$  constituents, respectively.

### 2.1 Modelling $V_s$ for sediments

We estimate  $\mu_e$  for cementless sediments using the Hertz-Mindlin rock physics model (Mindlin, 2021). The cementation model (Dvorkin & Nur, 1996) provides  $\mu_e$  for sediments with cements (e.g., ice and calcite) deposited at grain contacts or that surround

127 grains in contact. The models' equations can be found in Supporting Information Method  
 128 S1, Mindlin (2021), Dvorkin and Nur (1996), and Mavko et al. (2020). Model input pa-  
 129 rameters are mineral Poisson's ratio  $\nu_m$ , mineral bulk moduli  $\kappa_m$ , mineral shear mod-  
 130 uli  $\mu_m$ , cement fraction  $c_f$ , volume fraction of rough versus smooth grain contacts  $f$  (smooth  
 131 grain contacts allow elastic micro-scale slip during seismic wave propagation and rough  
 132 grain contacts do not), porosity  $\phi$ , effective stress  $P$ , and coordination number  $c_n$  (av-  
 133 erage number of grains contacting each other). We calculate mineral Poisson's ratio  $\nu_m$   
 134 using

$$\nu_m = \frac{3\kappa_m - 2\mu_m}{6\kappa_m + 2\mu_m}, \quad (3)$$

135 where  $\mu_m$  and  $\kappa_m$  are mineral shear and bulk moduli. Representative minerals within  
 136 Mars' subsurface and their respective  $\mu_m$  and  $\kappa_m$  are in Table 1. We treat basalt and  
 137 clay as single mineral constituents. We estimate porosity  $\phi$  changes with depth using

$$\phi = \phi_0 e^{-\frac{z}{k}}, \quad (4)$$

138 where  $z$ ,  $k$ , and  $\phi_0$  are depth in km, a porosity reduction constant scaled for Mars' grav-  
 139 itational field, and  $\phi$  at the surface, respectively. Clifford (1987) estimated  $k = 2.82$  km  
 140 based on scaling lunar observations; we consider values that range from 1 to 10 km. We  
 141 assume that  $\phi_0$  is between 0.3 and 0.5, consistent with studies that constrained  $\phi_0$  from  
 142 rover measurements and analog Earth studies (Golombek et al., 2018; Lewis et al., 2019;  
 143 Smrekar et al., 2019; Lognonné et al., 2020). Effective stress  $P$  is

$$P = \rho gh - P_f, \quad (5)$$

144 where  $g$ ,  $h$ , and  $P_f$  are gravitational acceleration on Mars (3.71 m/s<sup>2</sup>), depth, and fluid  
 145 pressures, respectively. Coordination number  $c_n$  is from Murphy (1982)

$$c_n = 20 - 34\phi + 14\phi^2. \quad (6)$$

146 We use the input parameters described above to calculate  $\mu_e$  from the rock physics model  
 147 equations, then  $V_s$  from equation 1.

**Table 1.** Mineral shear ( $\mu_m$ ) and bulk ( $\kappa_m$ ) moduli, and mineral density ( $\rho$ ) used in this study.

Mineral	$\mu_m$ (GPa)	$\kappa_m$ (GPa)	$\rho$ (kg/m <sup>3</sup> )	References
Calcite	28.2	71.6	2710	Mavko et al. (2020)
Basalt	40.0	80.0	2900	Christensen (1972); Heap (2019)
Clay	6.0	12.0	2650	Vanorio et al. (2003)
Halite	15.3	25.2	2160	Zong et al. (2017)
Ice	3.8	8.7	1220	Toksöz et al. (1976)
Plagioclase	25.6	75.6	2630	Woeber et al. (1963)

148 To compare measured and modeled  $V_s$ , we create a rock physics template that relates  
 149  $V_s$  to  $\phi$  (0-0.5), grain-contact friction (100% rough or smooth grain contacts), and  
 150 pore ice percentage (0-100%) for ice deposited at grain contacts or surrounding grains  
 151 in contact. Then, we identify the combinations of  $\phi$ , grain contact friction, and or pore  
 152 ice percentage that are consistent with the measured  $V_s$ . We also compare measured and  
 153 modeled  $V_s$  directly; these models assume a porosity reduction profile (equation 4) and

154 that pores host either 99% ice and 1% gas, 100% gas, 100% liquid water, 2% calcite ce-  
 155 ment and 98% gas, or 2% calcite cement and 98% liquid water. We model a cryosphere  
 156 as 99% ice and 1% gas because the cementation model breaks down for the 100% ice limit,  
 157 where 0% porosity introduces indeterminacy into the equations. We use a 10,000 real-  
 158 ization Monte Carlo simulation to incorporate input parameter uncertainties into the re-  
 159 sults from the models used for direct comparisons with measured  $V_s$ . During the Monte  
 160 Carlo simulation, we randomly select a new  $\phi$ -depth profile for each realization. Selected  
 161  $\phi$  values influence coordination number, bulk density, and effective stress.

## 162 2.2 Modeling $V_s$ for fractured rocks

163 We estimate  $\mu_e$  for fractured rocks using the self-consistent model of Berryman (1980).  
 164 The model's equations can be found in the Supporting Information Method S1, Berryman  
 165 (1980), and Mavko et al. (2020). The model's input parameters are  $\mu_m$ ,  $\kappa_m$ ,  $\phi$ , and pore  
 166 shape (defined by the aspect ratio,  $\alpha$  – i.e., the pore's short axis divided by the long axis).  
 167 We calculate  $\mu_e$  assuming that the fractures within a basalt contains either 100% gas,  
 168 100% water, 98% gas and 2% calcite cement, 98% water and 2% calcite cement, and 10-  
 169 100% ice. We then use  $\mu_e$  and  $\rho$  to calculate  $V_s$  from equation 1. We use these results  
 170 to create rock physics templates relating  $V_s$  to  $\phi$  (0.1-0.5),  $\alpha$  (0.01-1), and pore ice, wa-  
 171 ter, gas, and cement percentages. Last, we identify the ranges of  $\phi$ ,  $\alpha$ , and pore-filling  
 172 media that best explain measured  $V_s$ .

## 173 2.3 Sensitivity Analyses

174 We conduct sensitivity analyses to assess how model parameter uncertainties could  
 175 influence interpretations as well as to identify which rock properties are resolvable with  
 176 our models. Here, we first assume that  $\phi_0$  is 0.4,  $\phi$  exponentially decays with depth, gas  
 177 fills the pores, and there is no cement within the pores. Then, we vary a single input pa-  
 178 rameter to assess how its uncertainty influences modeled  $V_s$ . For granular media mod-  
 179 els, we vary mineralogy (100% basalt, plagioclase feldspar, or clay), coordination num-  
 180 ber (8, 12, 16, or 20), porosity decay constant (1, 2.82, or 10 km), cement type (98% gas  
 181 and 2% calcite, halite, or ice), and cement location (at grain contacts or entirely surrounds  
 182 grains). For fractured media models, we vary host rock composition (100% basalt, pla-  
 183 gioclase feldspar, or clay).

## 184 3 Results

### 185 3.1 Sediments

186 The ability to resolve changes in subsurface properties of sediment layers is most  
 187 affected by uncertainties in cement type and location, followed by  $\mu_m$  and  $\kappa_m$ ,  $c_n$ , and  
 188  $\phi$  (Figure 2). Assuming 100% basalt or plagioclase feldspar grains as representative of  
 189 the compositional diversity of igneous rocks (and all else equal) results in a  $V_s$  difference  
 190 of  $\sim 0.20$  km/s (Figure 2c), which is within the measured  $V_s$  uncertainties (Figure 1). Thus,  
 191 it is challenging to use the granular media rock physics models alone to distinguish be-  
 192 tween plausible igneous compositions. Clay layers may be seismically distinguishable from  
 193 igneous rock layers since the differences in their  $V_s$  predictions are 0.95 km/s and 0.72  
 194 km/s, respectively. Uncertainties in the porosity decay constant  $k$  (i.e., 1, 2.82, and 10)  
 195 produce a  $V_s$  range of  $\sim 0.28$  km/s (Figure 2b); this result implies that the assumed de-  
 196 cay constant does not significantly influence the interpretations of measured  $V_s$ . The range  
 197 for the modeled  $V_s$  difference for coordination numbers of 8, 12, 16, and 20 is 0.56 km/s,  
 198 which is within the uncertainty of measured  $V_s$  (Figure 2a). Assuming 2% calcite, ice,  
 199 and halite mineral cement produce  $V_s$  ranges of  $\sim 1.18$  km/s and  $\sim 0.64$  km/s for the ce-  
 200 ment at grain contacts versus on the grain surface, respectively (Figure 2d). Assuming  
 201 calcite and ice cement at grain surfaces predicts comparable velocities at all depths (i.e.,

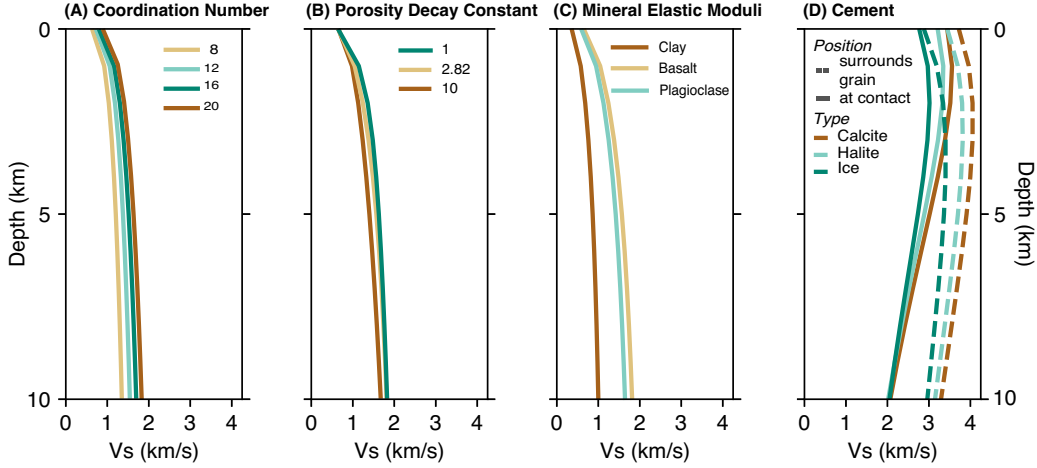


**Figure 2.** Effects of (A) coordination number, (B) porosity decay constant, (C) mineral moduli, and (D) cement type and location on  $V_s$ . We first assume that the subsurface comprises 100% basalt, porosity reduce exponentially with depth from  $\phi_0 = 0.4$ ,  $c_n$  is primarily controlled by  $\phi$  as constrained by the Murphy (1982) empirical relationship, and no mineral cements exist between grains and pores. Then, we only change the parameters being assessed in each graph to assess their influence on  $V_s$ .

202 within  $\sim 0.05$  km/s), implying that we can not distinguish between a few ( $< 2$ ) percent  
 203 pore ice and calcite cement based on  $V_s$  alone.

204 Figure 3 shows the granular media rock physics template relating  $V_s$ , porosity, pore-  
 205 filling media, and grain contact friction for modeled sediment layers. Measured  $V_s$  are  
 206 consistent with modeled  $V_s$  for sediments comprised of 100% rough-grain contacts and  
 207 sediments that host a few percent ice in their pores (Figure 3). Models for sediment with  
 208 100% rough-grain contacts are consistent with measured  $V_s$  if the sediments' porosities  
 209 are between 0.14 and 0.35. Models with 100% smooth grain contacts underpredict measured  
 210  $V_s$  for all porosities between 0 and 0.5. Models for sediments that host 10-18% ice  
 211 that surrounds grains in contact are consistent with the measured  $V_s$  if porosities are be-  
 212 tween 0.2-0.5. If pores are filled with 2% ice deposited at grain contacts, the porosities  
 213 need to be 0.4-0.5 to explain the measured  $V_s$ . The measured  $V_s$  are consistent with mod-  
 214 eled  $V_s$  for sediments with ice deposited at grain contacts if the pore-ice percentage is  
 215 less than 2% and porosities are higher than 0.37.

216 Assuming a porosity-depth reduction relationship defined by equation 4, where  $k =$   
 217 2.82 km, provides additional insights into the volume and type of pore-filling materials  
 218 that could explain measured  $V_s$  within the upper crust. Measured  $V_s$  are most consist-  
 219 ent with modeled  $V_s$  for a sediment with basalt grains and whose pores are filled with  
 220 gas or 2% calcite cement (Figure 4b and 4d). In general, Hertz-Mindlin rough-grained  
 221 models predict  $V_s$  with lower misfits than the smooth-grained models. The smooth-grained  
 222 model underpredicts  $V_s$  by 0.53 km/s for a gas-filled sediment layer in the upper crust  
 223 (Figure 4b). The liquid water saturated smooth-grained model underpredicts  $V_s$  by 0.61  
 224 km/s in the upper crust (Figure 4c). The rough-grained models for a gas or liquid water-  
 225 filled layer predicts higher  $V_s$  than the smooth-grained models in the upper crust by 0.4  
 226 km/s. Assuming that calcite cement fills 2% of the pores and liquid water or gas fills the  
 227 remaining 98% predict  $V_s$  within  $\pm \sim 0.42$  km/s of measured  $V_s$ , regardless of whether  
 228 the cement is deposited at grain contacts or surrounds grains (Figure 4d and 4e). As-  
 229 suming ice-saturated pores overpredicts measured  $V_s$  by 1.6 km/s (Figure 4a).



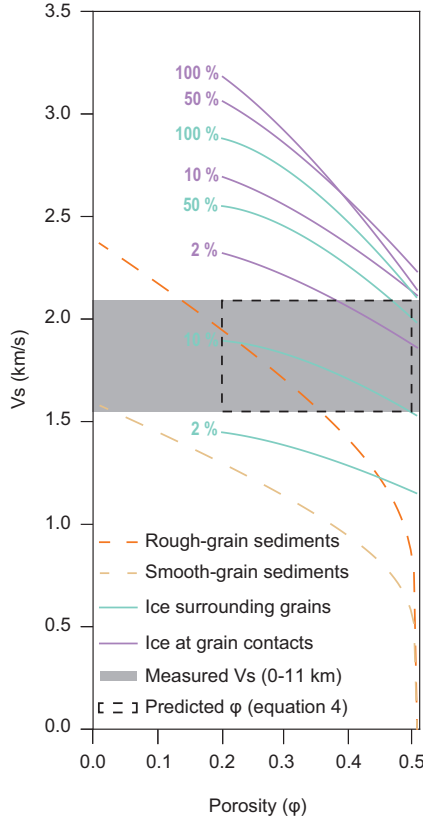


**Figure 3.** Rock physics template relating  $V_s$ , porosity, pore ice percentage, and sediments composed of 100% rough or smooth grain contacts.

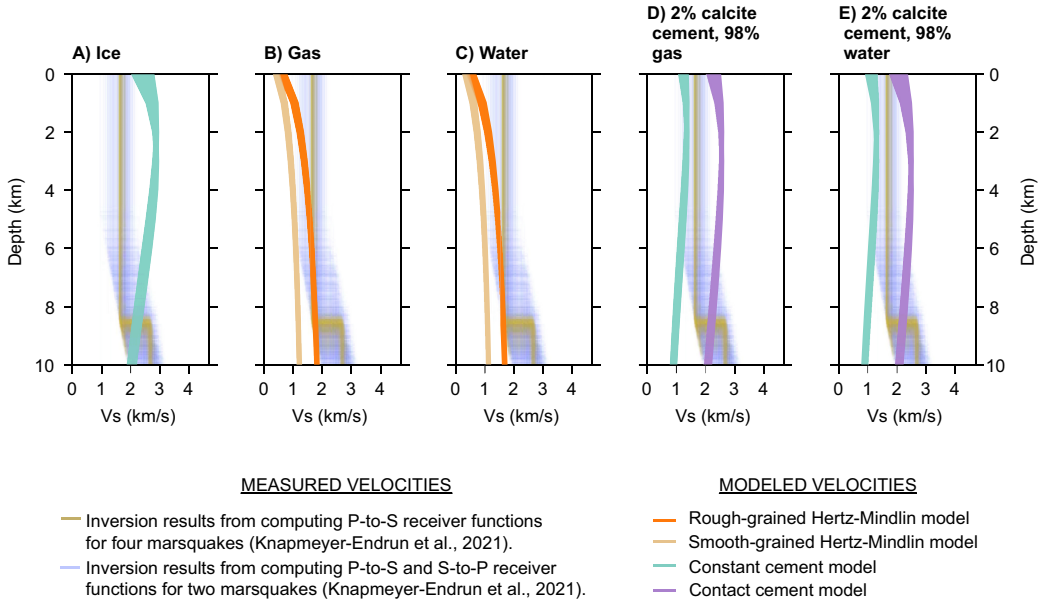


**Figure 4.** Comparisons of modeled and predicted  $V_s$  assuming basalt grains with pores filled with: A) 99% ice and 1% gas, B) 100% gas, C) 100% water, D) 2% calcite cement and 98% gas, and E) 2% calcite cement and 98% water.

230

### 3.2 Fractured Rocks

231

232

233

234

235

236

237

238

239

240

241

$V_s$  of fractured rocks are most sensitive to  $\alpha$ ,  $\phi$ , and elastic moduli of the host rock (Figures 5-7). As expected,  $V_s$  increases as porosity decreases and  $\alpha$  increases. The difference in  $V_s$  between basalt and other host rocks (e.g., plagioclase feldspar and clay) increases with decreasing porosity and increasing aspect ratio. A plagioclase host rock produces a difference of 0-0.5 km/s in  $V_s$  compared to a basalt host rock, for all pore-filling media (Figure 6). Thus, we can only distinguish between basalt and plagioclase rocks with  $V_s$  differences  $>0.3$  km/s. A clay versus basalt host rock lowers  $V_s$  by  $\sim 0.4$ - $2$  km/s for gas,  $\sim 0.15$ - $2$  km/s for liquid water,  $\sim 0.2$ - $2$  km/s for 2% calcite cement and 98% gas, and  $\sim 0.3$ - $2$  km/s for 2% calcite cement and 98% liquid water (Figure 7). Figure 7 shows the combinations of aspect ratio and porosities for when a clay and basalt host rock is resolvable (i.e., contour lines with  $V_s$  of at least 1.2 km/s).

242

243

244

245

246

247

248

249

250

251

252

253

254

255

A basalt host rock whose fractures are filled with varying percentages of ice, gas, water, and or calcite cement could explain the measured  $V_s$  in the upper and deeper crust. The upper crust could be filled with 100% gas, 100% liquid water, or 2% calcite cement with 98% gas or liquid water (Figure 5). Of these, a 100% gas-filled basalt (Figure 5a) produces the smallest number of  $\phi$ - $\alpha$  combinations ( $\phi = 0.1 - 0.47$  and  $\alpha = 0.03 - 1$ ) that could explain the measured  $V_s$ . A 2% calcite cemented basalt (Figure 5c-d) produces the largest combinations of  $\phi$ - $\alpha$  that could explain the measured  $V_s$ . Modeled  $V_s$  for basalts with ice that fills 20% to 60% of the pores are consistent with measured  $V_s$  if  $\phi$  is between 0.2 and 0.5. The measured  $V_s$  in the deeper crust are consistent with modeled  $V_s$  for a basalt filled with 100% gas or liquid water, 2% calcite cement with 98% gas or liquid water, or 10%-100% ice (Figures 5 and S1). A 100% gas-filled basalt (Figure 5a) produces the smallest number of  $\phi$ - $\alpha$  combinations ( $\phi = 0.1 - 0.4$  and  $\alpha = 0.04 - 1.0$ ) that could explain the measured  $V_s$ , while 60% ice-filled basalt host rock produces the largest number of  $\phi$ - $\alpha$  combinations ( $\phi = 0.1 - 0.5$  and  $\alpha = 0.01 - 1.0$ ) (Figure 5i).

256

## 4 Discussion

257

258

259

260

261

262

263

264

265

266

267

268

269

270

271

Our interpretations are guided by limitations associated with rock physics model assumptions, uncertainties in model parameters and measured  $V_s$ , available satellite and rover images, gravity-derived bulk density data, and heat flow models. The rock physics models provide end-member  $V_s$  estimates for the hypothesized stratigraphy (i.e., either sediments or fractured rocks filled with varying percentages of gas, liquid water, or ice and other mineral cements). Martian subsurface stratigraphy may include a mixture of fractured igneous rocks (e.g., basalts or 100% plagioclase feldspar) emplaced as volcanic lava flows or intrusions, brecciated sedimentary rocks, sands, and clays (Tanaka et al., 2014; Golombek et al., 2018; Pan et al., 2020; Warner et al., 2022). Thus, the measured  $V_s$  could be averages from several smaller rock and sediment layers that are not resolvable by the seismic velocity models (Knapmeyer-Endrun et al., 2021). Considering these limitations, our primary interpretations are that the upper crust comprises fractured basalt and cemented sediment layers whereas the deeper crust could comprises gas or water-filled fractured basalt with open, partially cemented fractures or more felsic igneous rock (represented here by 100% plagioclase feldspar) layers with 0-23% porosity.

272

### 4.1 Fractured rocks and cemented sediments within the upper crust

273

274

275

276

277

278

279

Our comparisons of measured and modeled  $V_s$  suggest that gas-filled fractured rock and cemented sediment layers may coexist within the upper crust. We interpret that the upper crust is gas-filled because temperatures in the upper crust would freeze water (Clifford et al., 2010). Sediments filled with 2% cement and 98% gas and basalts filled with gas are possible within the upper crust since their modeled  $V_s$  are consistent with measured  $V_s$  when we parameterize the models with the gravity-derived porosity range (0.10-0.23) (Figure 4) (Goossens et al., 2017). The coexistence of the gas-filled basalt and weakly-

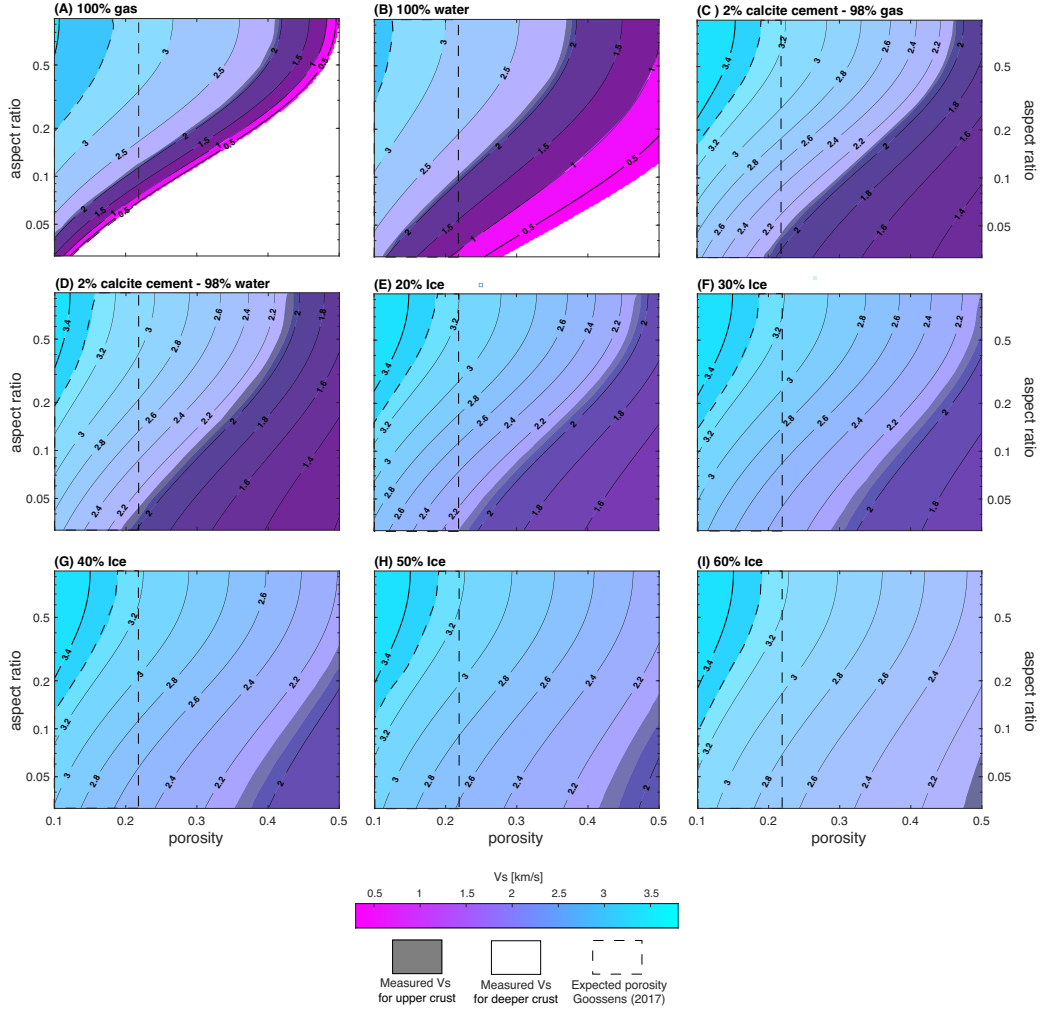


**Figure 5.** Rock physics template showing the  $V_s$  relationship between  $\alpha$  (0.01-1.00),  $\phi$  (0.1-0.5), varying pore-filling media, and varying pore-filling ice percentage. The black shading shows  $V_s$  for the upper crust; the white shading shows  $V_s$  for the deeper crust. The pore spaces are filled with either (A) gas, (B) water, (C) 2% calcite cement and 98% gas, (D) 2% calcite cement and 98% water, or (E) 20%, (F) 30%, (G) 40%, (H) 50%, or (I) 60% ice. Y-axis is logarithmic.

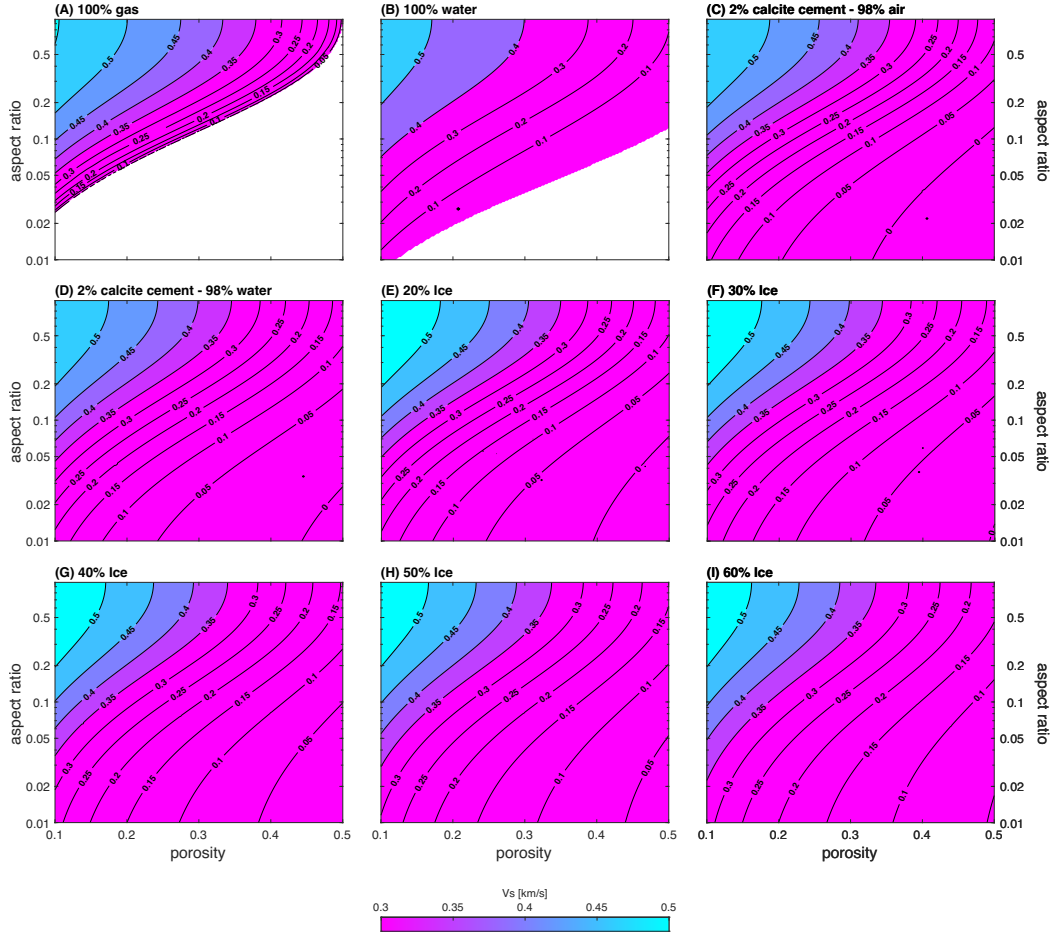


**Figure 6.** Rock physics sensitivity template showing the  $V_s$  difference between a basalt and plagioclase feldspar host rock.  $V_s$  changes with  $\alpha$  (0.01-1.00),  $\phi$  (0.1-1), and pore-filling media. The pores are filled with either (A) gas, (B) water, (C) 2% calcite cement and 98% gas, (D) 2% calcite cement and 98% water, or (E) 20%, (F) 30% , (G) 40%, (H) 50%, or (I) 60% ice. Y-axis is logarithmic.

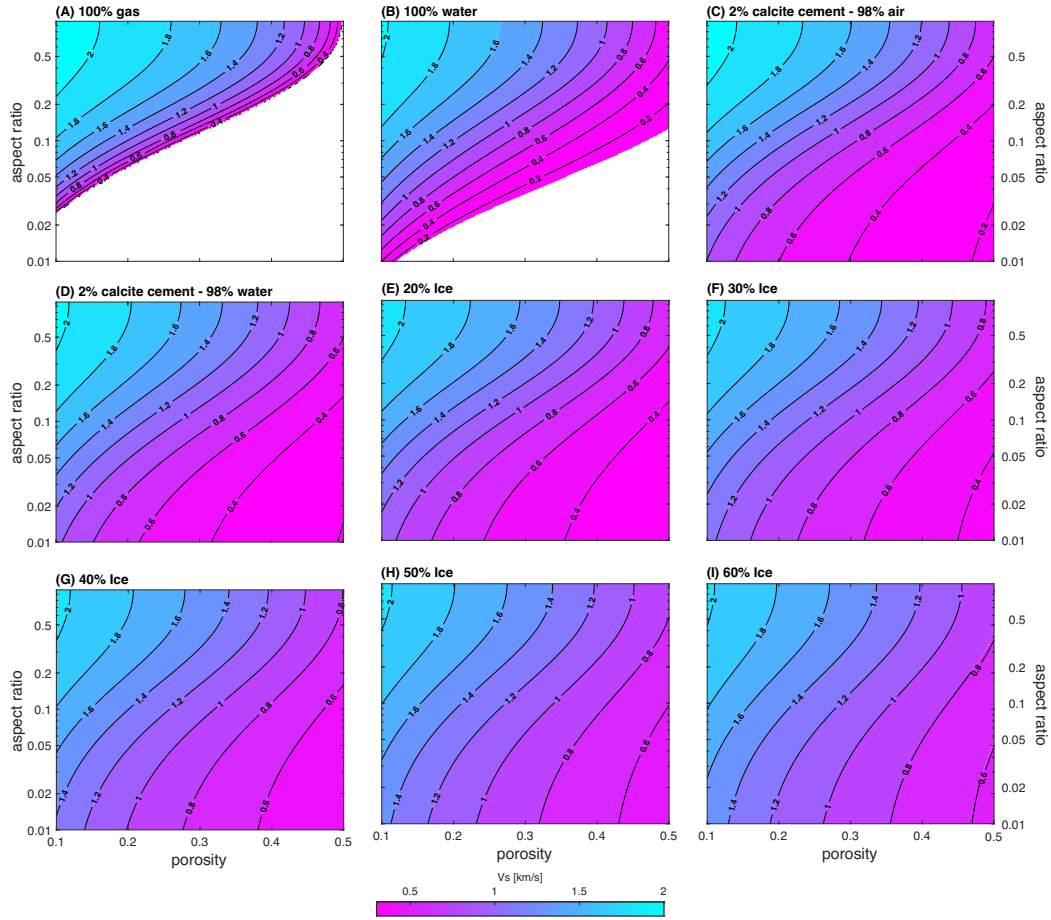


**Figure 7.** Rock physics sensitivity template showing the  $V_s$  difference between a basalt and clay host rock.  $V_s$  changes with  $\alpha$  (0.01-1.00),  $\phi$  (0.1-0.5), and pore-filling material. The pores are filled with either (A) gas, (B) water, (C) 2% calcite cement and 98% gas, (D) 2% calcite cement and 98% water, or (E) 20%, (F) 30% , (G) 40%, (H) 50%, or (I) 60% ice. Y-axis is logarithmic.

280 cemented sediment layers would be resolved as one seismic velocity layer in seismic ve-  
 281 locity models since differences in the layers'  $V_s$  would not produce a large impedance con-  
 282 trasts. Additional support for the potential coexistence of igneous rock and sediment lay-  
 283 ers in the upper crust comes from (1) Martian meteorites and images of surface-exposed  
 284 stratigraphic columns that evidence basalts, sandstones, and sediments in the upper 1  
 285 km of the crust (Carr & Head, 2002; Edwards et al., 2011; McSween, 2015; Golombek  
 286 et al., 2018; Hobiger et al., 2021; Knapmeyer-Endrun et al., 2021) and (2) Insight-derived  
 287 high-resolution seismic velocities that are consistent with gas-filled basalt and sediment  
 288 layers down to 0.3 km below the surface of the landing site (Hobiger et al., 2021; Wright  
 289 et al., 2022). Other layers with different lithologies and pore-filling media, and hence dif-  
 290 ferent  $V_s$ , may exist within the upper crust. If so, these layers are likely too thin to be  
 291 detected by the longer period marsquake waves used by Knapmeyer-Endrun et al. (2021)  
 292 to constrain the  $V_s$ -depth structure.

## 293 4.2 No ice-saturated cryosphere in the upper crust

294 There is likely no cryosphere within the upper crust, beneath InSight. The lack of  
 295 a cryosphere is indicated by observations that when ice-filled, the granular media mod-  
 296 els overpredict measured  $V_s$  by 0.5-2 km/s (Figure 4a) and that, for fractured basalts,  
 297 there are no modeled combinations of porosity and pore shape that would explain the  
 298 measured  $V_s$  if we restrict porosity to 0.10-0.23, as estimated by Goossens et al. (2017)  
 299 (Figure 5e-i). One possibility not captured by our models is that there exists mushy ice  
 300 (i.e., mix of soft, snow-like, ice and brine) within the pores of rocks and sediments de-  
 301 posited at depths greater than a few hundred meters, depending on regional heat flow.  
 302 Detecting a mushy ice may require improved constraints on attenuation beneath InSight  
 303 and developing models connecting seismic velocities, attenuation, and mushy ice concen-  
 304 trations (Dou et al., 2017). This can be done using lab and permafrost experiments. Seis-  
 305 mic attenuation may also provide constraints on fracture orientations (Li et al., 2022).

## 306 4.3 Mineralogy, pore collapse, and pore-filling media in the deeper crust

307 Our model comparisons, the reliability of fractured media models for predicting  $V_s$   
 308 of very low  $\phi$  (<3%) basalts, and differences in the effective pressures and heat flow be-  
 309 tween Earth and Mars lead us to interpret that, if basaltic, the deeper crust has 10-23%  
 310 porosity. The measured  $V_s$  in Mars' deeper crust are 0.4-1.7 km/s lower than  $V_s$  for mod-  
 311 eled unfractured basalts. Fractured media rock physics models successfully predict  $V_s$   
 312 of very low  $\phi$  (<3%) basalts with as little as 0-2% misfit (Tsuji & Iturrino, 2008). Our  
 313 model predicts  $V_s$  of  $\sim 3.7$  km/s for unfractured ( $\phi=0$ ) Martian basalts, assuming the  
 314 mineral elastic moduli and densities listed in Table 1. If the deeper crust is basaltic and  
 315 pores are filled with gas, liquid water, or 2% cement and 98% gas or liquid water, Mars'  
 316 comparatively lower  $V_s$  may be explained by basalt layers with  $\alpha=0.15-0.8$ ,  $\phi=0.10-0.23$   
 317 (Figures 1, 5), and bulk density  $\rho=2,318-2,713$  kg/m<sup>3</sup> (equation 2). These  $\rho$  and hence  
 318  $\phi$  ranges are consistent with Goossens et al. (2017) gravity-derived bulk density and poros-  
 319 ity ranges for the deeper crust. The porosity of Earth ocean basalts reduce by  $\sim 90\%$  from  
 320 0-6 km depth (Chen et al., 2020). At 6 km below the surface of Mars, assuming  $\phi = 0.10$   
 321 (the lower  $\phi$  limit proposed by Goossens et al. (2017)) and gas or liquid water fills the  
 322 host rock, Earth's effective pressure is  $\sim 3$  times greater than Mars' (equation 5). Earth's  
 323 average heat flux is  $\sim 4.8$  times greater than Mars' average (Davies & Davies, 2010; Parro  
 324 et al., 2017). Manning and Ingebritsen (1999) estimates that viscous creep-induced pore  
 325 collapse occurs at an average depth of  $\sim 12$  km on Earth. Thus, we infer that Mars' lower  
 326 effective stress, heat flow, and gravitational acceleration would cause elastic pore closure  
 327 to occur at depths deeper than 12 km. Our findings and interpretations imply that a basaltic  
 328 host rock would require 10-23% porosity and effective pressure-induced pore collapse may  
 329 occur at the same depth as the second seismic discontinuity, located at the base of the  
 330 deeper crust. This interpreted depth of pore collapse does not preclude the possibility

331 that thermally-activated pore collapse occurred in the deeper crust in the past (Gyalay  
 332 et al., 2020), and currently open pores may have been created by subsequent surface im-  
 333 pacts or other stresses.

334 Our model comparisons show that the  $V_s$  in the deeper crust is also consistent with  
 335 a plagioclase feldspar host rock with 0-23% porosity. Wieczorek et al. (2022) proposed  
 336 that Mars'  $V_s$  may be lower than unfractured basalt's because the Martian crust com-  
 337 prises more felsic, feldspar-dominated igneous rocks whose density and shear moduli, and  
 338 hence  $V_s$ , are lower than those of basalt. We represent the felsic end-member igneous rock  
 339 as a 100% plagioclase feldspar host rock. Our modeled  $V_s$  of an unfractured plagioclase  
 340 host rock is  $\sim 3.1$  km/s, which falls in the upper 75% quartile of the InSight-derived  $V_s$   
 341 range for the deeper crust (Figure 1) and supports the idea that the measured  $V_s$  on Mars  
 342 could be explained by zero porosity (unfractured) plagioclase feldspar. We note that the  
 343 two groups of InSight-derived measured  $V_s$  on Mars, based on P-S receiver function in-  
 344 version from four versus two marsquakes, overlap at  $\sim 2.6$ - $2.75$  km/s (Figure 1). If the  
 345 deeper crust comprises 100% plagioclase and it is fractured and filled with gas, liquid  
 346 water, or 2% cement and 98% gas or liquid water, the measured  $V_s$  in the overlapping  
 347 range may also be explained by layers of 100% plagioclase feldspar whose  $\alpha=0.07$ - $0.97$ ,  
 348  $\phi=0.10$ - $0.23$  (Figures 1, 6, S2), and bulk density  $\rho=2,277$ - $2,601$  kg/m<sup>3</sup> (equation 2). These  
 349  $\phi$  and  $\rho$  ranges are consistent with Goossens et al. (2017) gravity-derived  $\phi$  and  $\rho$  ranges  
 350 for the deeper crust. If the host rock is 100% plagioclase and unfractured, viscous creep-  
 351 induced pore closure may occur at the same depth as the shallower seismic discontinu-  
 352 ity, located at the top of the deeper crust. If up to 23% porosity exists, the onset of vis-  
 353 cuous creep-induced pore closure may occur at the same depth of the deeper seismic dis-  
 354 continuity, located at the base of the deeper crust; the porosity may also be due to post-  
 355 pore-closure impact fracturing or other stresses. Together, our analyses suggest that if  
 356 the host rock is 100% plagioclase, the deeper crust is unfractured with pore closure oc-  
 357 ccurring at the shallower seismic discontinuity or hosts up to 23% porosity, which is filled  
 358 with gas, liquid water, or 2% cement and 98% gas or liquid water. In the latter scenario,  
 359 pore closure occurs at the deeper seismic discontinuity.

360 If porosity exists, pores in the deeper crust could be filled with gas, liquid water,  
 361 or 2% cement and 98% gas or liquid water. We can not distinguish between gas and water-  
 362 filled pores in the deeper crust since the  $V_s$  difference between a gas- and water-filled host  
 363 rock at this depth is less than 0.1 km/s (Figure 5a-d, S2) and the modeled geothermal  
 364 gradient on Mars suggest that liquid water could be stable beneath 8 km (Clifford et al.,  
 365 2010). Though the measured  $V_s$  are consistent with a fractured host rock whose pores  
 366 are ice filled, we infer that ice does not fill the pores because temperatures in the deeper  
 367 crust are too high to freeze water (Clifford et al., 2010). Pores are likely filled with at  
 368 least 2% cement because models for a 2% calcite cemented crust with 98% gas or liq-  
 369 uid water are consistent with measured  $V_s$  within the gravity-derived porosity range (0.10-  
 370 0.23) (Goossens et al., 2017). Apart from calcite, other non-ice mineral cements could  
 371 exist within the pores since the differences between the elastic mineral moduli of calcite  
 372 and other expected cements within Mars' crust (Table 1) result in  $V_s$  differences no greater  
 373 than  $\sim 0.1$  km/s if cement fills 2% of the pores. Cements usually precipitate from liquid  
 374 water solutions. If the source of liquid water in the deeper crust is from the surface or  
 375 upper crust, this liquid water needed to percolate to the deeper crust before tempera-  
 376 tures in the upper crust became cold enough to freeze liquid water. Modest amounts of  
 377 deeper crustal liquid water could also be supplied by intrusive magma below or within  
 378 the deeper crust (Black et al., 2022).

## 379 5 Conclusions

380 This study uses rock physics models and shear wave velocities  $V_s$  to constrain the  
 381 volume and distribution of subsurface liquid water, mineral cements, and lithology be-  
 382 neath InSight on Mars. The upper crust (0-8 km) most likely comprises gas-filled frac-

383 tured basalts and minimally cemented (up to 2% in pores) sediment layers. Measured  
 384  $V_s$  in the upper crust are too low for an ice-saturated cryosphere layer. The deeper crust  
 385 (8-20 km) comprises consolidated basalts or plagioclase feldspar whose fractures have  
 386 not closed entirely and may be filled with gas, water, or 2% non-ice mineral cements and  
 387 98% gas or liquid water. The range of measured  $V_s$  in the deeper crust are also consis-  
 388 tent with an unfractured plagioclase feldspar. The presence and quantity of liquid wa-  
 389 ter in the pores would be better resolved by integrating our results with constraints from  
 390 compressional wave velocities and seismic wave attenuation.

391 The results of this study have implications for the thermal and hydrogeological histo-  
 392 ry of the Martian subsurface, beneath InSight. Pores within the deeper crust could re-  
 393 main open because the processes promoting porosity creation (e.g., chemical reactions  
 394 such as dissolution or impact cratering) are more dominant than thermally-activated vis-  
 395 cous creep-induced pore collapse. Pores could also be currently open because they were  
 396 created by impacts after the rocks experienced pore collapse induced by viscous creep.  
 397 Open pores could host liquid water that, if sourced from the surface or the upper crust,  
 398 percolated to the deeper crust before temperatures became colder, freezing the water on  
 399 its way down. Alternatively, liquid water could be introduced to the deeper crust via mag-  
 400 matic processes.

## 401 6 Data Availability Statement

402 No new data were used in this study. The InSight-derived seismic velocities that  
 403 we used in this study are available in Knapmeyer-Endrun et al. (2021).

## 404 Acknowledgments

405 R. Kilburn, J. Dasent, and V. Wright acknowledge support from National Science  
 406 Foundation grant 2136301. M. Manga acknowledges support from the CIFAR Earth 4D  
 407 program and NASA grant 80NSSC19K0545. The authors thank NASA and the InSight  
 408 team for their dedication, hard work, and vision, especially during this time when COVID-  
 409 19 is real. The authors also thank the Mars, No Structure, Just Vibes retreat for pro-  
 410 viding a welcoming environment and support during the writing of this manuscript.

## 411 References

- 412 Adam, L., van Wijk, K., Otheim, T., & Batzle, M. (2013). Changes in elastic wave  
 413 velocity and rock microstructure due to basalt-CO<sub>2</sub>-water reactions. *Journal of*  
 414 *Geophysical Research: Solid Earth*, *118*(8), 4039–4047. doi: [https://doi.org/10](https://doi.org/10.1002/jgrb.50302)  
 415 [.1002/jgrb.50302](https://doi.org/10.1002/jgrb.50302)
- 416 Baker, V. R. (2006). Geomorphological evidence for water on Mars. *Elements*, *2*(3),  
 417 139–143. doi: <https://doi.org/10.2113/gselements.2.3.139>
- 418 Berryman, J. G. (1980). Long-wavelength propagation in composite elastic media  
 419 I. Spherical inclusions II. Ellipsoidal inclusions. *The Journal of the Acoustical*  
 420 *Society of America*, *68*(6), 1820–1831. doi: <https://doi.org/10.1121/1.385172>
- 421 Bibring, J.-P., Langevin, Y., Gendrin, A., Gondet, B., Poulet, F., Berthé, M., ...  
 422 others (2005). Mars surface diversity as revealed by the OMEGA/Mars Ex-  
 423 press observations. *Science*, *307*(5715), 1576–1581. doi: [https://doi.org/](https://doi.org/10.1126/science.1108806)  
 424 [10.1126/science.1108806](https://doi.org/10.1126/science.1108806)
- 425 Black, B. A., Manga, M., Ojha, L., Longpré, M.-A., Karunatillake, S., & Hlinka, L.  
 426 (2022). The history of water in Martian magmas from thorium maps. *Geophys-*  
 427 *ical Research Letters*, *49*(11), e2022GL098061. doi: [https://doi.org/10.1029/](https://doi.org/10.1029/2022GL098061)  
 428 [2022GL098061](https://doi.org/10.1029/2022GL098061)
- 429 Boynton, W., Ming, D., Kounaves, S., Young, S., Arvidson, R., Hecht, M., ... oth-  
 430 ers (2009). Evidence for calcium carbonate at the Mars Phoenix landing site.



- 431 *Science*, 325(5936), 61–64. doi: <https://doi.org/10.1126/science.1172768>
- 432 Burr, D. M., Grier, J. A., McEwen, A. S., & Keszthelyi, L. P. (2002). Re-
- 433 peated aqueous flooding from the cerberus fossae: Evidence for very re-
- 434 cently extant, deep groundwater on mars. *Icarus*, 159(1), 53–73. doi:
- 435 <https://doi.org/10.1006/icar.2002.6921>
- 436 Carr, M. (1987). Water on Mars. *Nature*, 326(6108), 30–35. doi: [https://doi.org/](https://doi.org/10.1038/326030a0)
- 437 [10.1038/326030a0](https://doi.org/10.1038/326030a0)
- 438 Carr, M., & Head, J. (2002). Elevations of water-worn features on Mars: Implica-
- 439 tions for circulation of groundwater. *Journal of Geophysical Research: Planets*,
- 440 107(E12), 14–1. doi: <https://doi.org/10.1029/2002JE001845>
- 441 Carr, M., & Head, J. (2003). Oceans on Mars: An assessment of the observational
- 442 evidence and possible fate. *Journal of Geophysical Research: Planets*, 108(E5).
- 443 doi: <https://doi.org/10.1029/2002JE001963>
- 444 Carr, M., & Head, J. (2019). Mars: Formation and fate of a frozen Hesperian ocean.
- 445 *Icarus*, 319, 433–443. doi: <https://doi.org/10.1016/j.icarus.2018.08.021>
- 446 Chen, J., Kuang, X., & Zheng, C. (2020). An empirical porosity–depth model for
- 447 Earth’s crust. *Hydrogeology Journal*, 28(7), 2331–2339. doi: [10.1007/s10040-](https://doi.org/10.1007/s10040-020-02214-x)
- 448 [-020-02214-x](https://doi.org/10.1007/s10040-020-02214-x)
- 449 Christensen, N. I. (1972). Compressional and shear wave velocities at pressures to
- 450 10 kilobars for basalts from the East Pacific Rise. *Geophysical Journal Interna-*
- 451 *tional*, 28(5), 425–429. doi: [https://doi.org/10.1111/j.1365-246X.1972.tb06140-](https://doi.org/10.1111/j.1365-246X.1972.tb06140.x)
- 452 [.x](https://doi.org/10.1111/j.1365-246X.1972.tb06140.x)
- 453 Citron, R. I., Manga, M., & Hemingway, D. J. (2018). Timing of oceans on Mars
- 454 from shoreline deformation. *Nature*, 555(7698), 643–646. doi: [https://doi.org/](https://doi.org/10.1038/nature26144)
- 455 [10.1038/nature26144](https://doi.org/10.1038/nature26144)
- 456 Clifford, S., Lasue, J., Heggy, E., Boisson, J., McGovern, P., & Max, M. D. (2010).
- 457 Depth of the Martian cryosphere: Revised estimates and implications for the
- 458 existence and detection of subpermafrost groundwater. *Journal of Geophysical*
- 459 *Research: Planets*, 115(E7). doi: <https://doi.org/10.1029/2009JE003462>
- 460 Clifford, S. M. (1987). Mars: Crustal Pore Volume, Cryospheric Depth, and the
- 461 Global Occurrence of Groundwater. In V. Baker et al. (Eds.), *Meca symposium*
- 462 *on mars: Evolution of its climate and atmosphere* (p. 32).
- 463 Clifford, S. M. (1993). A model for the hydrologic and climatic behavior of water
- 464 on Mars. *Journal of Geophysical Research: Planets*, 98(E6), 10973–11016. doi:
- 465 <https://doi.org/10.1029/93JE00225>
- 466 Clifford, S. M. (1997). The Origin of the Martian Intercrater Plains: The Role of
- 467 Liquefaction from Impact and Tectonic-induced Seismicity. In *Lunar and plan-*
- 468 *etary science conference* (p. 241).
- 469 Clifford, S. M., & Parker, T. J. (2001). The evolution of the Martian hydro-
- 470 sphere: Implications for the fate of a primordial ocean and the current state
- 471 of the northern plains. *Icarus*, 154(1), 40–79. doi: [https://doi.org/10.1006/](https://doi.org/10.1006/icar.2001.6671)
- 472 [icar.2001.6671](https://doi.org/10.1006/icar.2001.6671)
- 473 Colaprete, A., & Jakosky, B. M. (1998). Ice flow and rock glaciers on Mars. *Journal*
- 474 *of Geophysical Research: Planets*, 103(E3), 5897–5909. doi: [https://doi.org/10](https://doi.org/10.1029/97JE03371)
- 475 [.1029/97JE03371](https://doi.org/10.1029/97JE03371)
- 476 Davies, J. H., & Davies, D. R. (2010). Earth’s surface heat flux. *Solid Earth*, 1(1),
- 477 5–24. doi: [10.5194/se-1-5-2010](https://doi.org/10.5194/se-1-5-2010)
- 478 Di Achille, G., & Hynes, B. M. (2010). Ancient ocean on Mars supported by global
- 479 distribution of deltas and valleys. *Nature Geoscience*, 3(7), 459–463. doi:
- 480 <https://doi.org/10.1038/ngeo891>
- 481 Dou, S., Nakagawa, S., Dreger, D., & Ajo-Franklin, J. (2017). An effective-medium
- 482 model for P-wave velocities of saturated, unconsolidated saline permafrost.
- 483 *Geophysics*, 82(3), EN33–EN50. doi: <https://doi.org/10.1190/geo2016-0474.1>
- 484 Dvorkin, J., & Nur, A. (1996). Elasticity of high-porosity sandstones: Theory for
- 485 two North Sea data sets. *Geophysics*, 61(5), 1363–1370. doi: [https://doi.org/](https://doi.org/10.1190/geo2016-0474.1)

- 486 10.1190/1.1444059  
 487 Edwards, C., Nowicki, K., Christensen, P., Hill, J., Gorelick, N., & Murray, K.  
 488 (2011). Mosaicking of global planetary image datasets: 1. Techniques and  
 489 data processing for Thermal Emission Imaging System (THEMIS) multi-  
 490 spectral data. *Journal of Geophysical Research: Planets*, 116(E10). doi:  
 491 <https://doi.org/10.1029/2010JE003755>
- 492 Golombek, M., Grott, M., Kargl, G., Andrade, J., Marshall, J., Warner, N., ... oth-  
 493 ers (2018). Geology and physical properties investigations by the InSight  
 494 lander. *Space Science Reviews*, 214(5), 1–52. doi: [https://doi.org/10.1007/  
 495 s11214-018-0512-7](https://doi.org/10.1007/s11214-018-0512-7)
- 496 Goossens, S., Sabaka, T. J., Genova, A., Mazarico, E., Nicholas, J. B., & Neumann,  
 497 G. A. (2017). Evidence for a low bulk crustal density for Mars from grav-  
 498 ity and topography. *Geophysical research letters*, 44(15), 7686–7694. doi:  
 499 <https://doi.org/10.1002/2017GL074172>
- 500 Gyalay, S., Nimmo, F., Plesa, A.-C., & Wiczorek, M. (2020). Constraints on ther-  
 501 mal history of mars from depth of pore closure below InSight. *Geophysical Re-  
 502 search Letters*, 47(16), e2020GL088653.
- 503 Halevy, I., & Schrag, D. (2009). Sulfur dioxide inhibits calcium carbonate precip-  
 504 itation: Implications for early Mars and Earth. *Geophysical Research Letters*,  
 505 36(23). doi: <https://doi.org/10.1029/2009GL040792>
- 506 Heap, M. J. (2019). P-and S-wave velocity of dry, water-saturated, and frozen  
 507 basalt: Implications for the interpretation of Martian seismic data. *Icarus*,  
 508 330, 11–15. doi: <https://doi.org/10.1016/j.icarus.2019.04.020>
- 509 Hobiger, M., Hallo, M., Schmelzbach, C., Stähler, S., Fäh, D., Giardini, D., ... oth-  
 510 ers (2021). The shallow structure of Mars at the InSight landing site from  
 511 inversion of ambient vibrations. *Nature communications*, 12(1), 1–13. doi:  
 512 <https://doi.org/10.1038/s41467-021-26957-7>
- 513 Jakosky, B. M. (2021). Atmospheric loss to space and the history of water on Mars.  
 514 *Annual Review of Earth and Planetary Sciences*, 49, 71–93. doi: [https://doi/  
 515 .org/10.1146/annurev-earth-062420-052845](https://doi.org/10.1146/annurev-earth-062420-052845)
- 516 Jenkins, J., Johnson, D., La Ragione, L., & Makse, H. (2005). Fluctuations and  
 517 the effective moduli of an isotropic, random aggregate of identical, frictionless  
 518 spheres. *Journal of the Mechanics and Physics of Solids*, 53(1), 197–225. doi:  
 519 <https://doi.org/10.1016/j.jmps.2004.06.002>
- 520 Knapmeyer-Endrun, B., Panning, M. P., Bissig, F., Joshi, R., Khan, A., Kim, D.,  
 521 ... others (2021). Thickness and structure of the martian crust from InSight  
 522 seismic data. *Science*, 373(6553), 438–443. doi: [https://doi.org/10.1126/  
 523 science.abf8966](https://doi.org/10.1126/science.abf8966)
- 524 Lewis, K. W., Peters, S., Gonter, K., Morrison, S., Schmerr, N., Vasavada, A. R.,  
 525 & Gabriel, T. (2019). A surface gravity traverse on Mars indicates  
 526 low bedrock density at Gale crater. *Science*, 363(6426), 535–537. doi:  
 527 <https://doi.org/10.1126/science.abf8966>
- 528 Li, J., Beghein, C., Wookey, J., Davis, P., Lognonné, P., Schimmel, M., ...  
 529 Banerdt, W. B. (2022). Evidence for crustal seismic anisotropy at the In-  
 530 Sight lander site. *Earth and Planetary Science Letters*, 593, 117654. doi:  
 531 <https://doi.org/10.1016/j.epsl.2022.117654>
- 532 Lognonné, P., Banerdt, W., Pike, W., Giardini, D., Christensen, U., Garcia, R. F.,  
 533 ... others (2020). Constraints on the shallow elastic and anelastic structure  
 534 of Mars from InSight seismic data. *Nature Geoscience*, 13(3), 213–220. doi:  
 535 <https://doi.org/10.1038/s41561-020-0536-y>
- 536 Manga, M. (2004). Martian floods at Cerberus Fossae can be produced by ground-  
 537 water discharge. *Geophysical Research Letters*, 31(2). doi: [https://doi.org/10.  
 538 .1029/2003GL018958](https://doi.org/10.1029/2003GL018958)
- 539 Manga, M., & Wright, V. (2021). No Cryosphere-Confined Aquifer Below InSight on  
 540 Mars. *Geophysical Research Letters*, 48(8), e2021GL093127. doi: <https://doi.org/10.1029/2021GL093127>

- 541 .org/10.1029/2021GL093127
- 542 Manning, C., & Ingebritsen, S. (1999). Permeability of the continental crust: Impli-  
 543 cations of geothermal data and metamorphic systems. *Reviews of Geophysics*,  
 544 *37*(1), 127–150. doi: <https://doi.org/10.1029/1998RG900002>
- 545 Mavko, G., Mukerji, T., & Dvorkin, J. (2020). *The rock physics handbook*. Cam-  
 546 bridge university press. doi: <https://doi.org/10.1017/9781108333016>
- 547 McSween, H. Y. (2015). Petrology on Mars. *American Mineralogist*, *100*(11-12),  
 548 2380–2395. doi: <https://doi.org/10.2138/am-2015-5257>
- 549 Mindlin, R. D. (2021). Compliance of Elastic Bodies in Contact. *Journal of Applied*  
 550 *Mechanics*, *16*(3), 259–268. doi: 10.1115/1.4009973
- 551 Murphy, W. F. (1982). *Effects of microstructure and pore fluids on the acoustic*  
 552 *properties of granular sedimentary materials* (Unpublished doctoral disserta-  
 553 tion). Stanford University.
- 554 Mustard, J. F. (2019). Sequestration of volatiles in the Martian crust through hy-  
 555 drated minerals: A significant planetary reservoir of water. In *Volatiles in the*  
 556 *martian crust* (pp. 247–263). Elsevier. doi: [https://doi.org/10.1016/B978-0-12-](https://doi.org/10.1016/B978-0-12-804191-8.00008-8)  
 557 [804191-8.00008-8](https://doi.org/10.1016/B978-0-12-804191-8.00008-8)
- 558 Nazari-Sharabian, M., Aghababaei, M., Karakouzian, M., & Karami, M. (2020). Wa-  
 559 ter on Mars—a literature review. *Galaxies*, *8*(2), 40. doi: [https://doi.org/10](https://doi.org/10.3390/galaxies8020040)  
 560 [.3390/galaxies8020040](https://doi.org/10.3390/galaxies8020040)
- 561 Orosei, R., Lauro, S., Pettinelli, E., Cicchetti, A., Coradini, M., Cosciotti, B., ...  
 562 others (2018). Radar evidence of subglacial liquid water on Mars. *Science*,  
 563 *361*(6401), 490–493. doi: <https://doi.org/10.1126/science.aar7268>
- 564 Pan, L., Quantin-Nataf, C., Tauzin, B., Michaut, C., Golombek, M., Lognonné,  
 565 P., ... others (2020). Crust stratigraphy and heterogeneities of the first  
 566 kilometers at the dichotomy boundary in western Elysium Planitia and impli-  
 567 cations for InSight lander. *Icarus*, *338*, 113511. doi: [https://doi.org/10.1016/](https://doi.org/10.1016/j.icarus.2019.113511)  
 568 [j.icarus.2019.113511](https://doi.org/10.1016/j.icarus.2019.113511)
- 569 Parro, L. M., Jiménez-Díaz, A., Mansilla, F., & Ruiz, J. (2017). Present-day heat  
 570 flow model of Mars. *Scientific reports*, *7*(1), 1–9. doi: [https://doi.org/10.1038/](https://doi.org/10.1038/srep45629)  
 571 [srep45629](https://doi.org/10.1038/srep45629)
- 572 Rodriguez, J. A. P., Kargel, J. S., Baker, V. R., Gulick, V. C., Berman, D. C.,  
 573 Fairén, A. G., ... others (2015). Martian outflow channels: How did their  
 574 source aquifers form and why did they drain so rapidly? *Scientific reports*,  
 575 *5*(1), 1–10. doi: <https://doi.org/10.1029/2003GL018958>
- 576 Scheller, E., Ehlmann, B., Hu, R., Adams, D., & Yung, Y. (2021). Long-term drying  
 577 of Mars by sequestration of ocean-scale volumes of water in the crust. *Science*,  
 578 *372*(6537), 56–62. doi: <https://doi.org/10.1126/science.abc7717>
- 579 Smrekar, S. E., Lognonné, P., Spohn, T., Banerdt, W. B., Breuer, D., Christensen,  
 580 U., ... others (2019). Pre-mission InSights on the interior of Mars. *Space Sci-*  
 581 *ence Reviews*, *215*(1), 1–72. doi: <https://doi.org/10.1007/s11214-018-0563-9>
- 582 Tanaka, K. L., Skinner, J. A., Dohm, J. M., Irwin III, R. P., Kolb, E. J., Fortezzo,  
 583 C. M., ... Hare, T. M. (2014). *Geologic map of Mars* (Report No. 3292).  
 584 Reston, VA. doi: 10.3133/sim3292
- 585 Te Wu, T. (1966). The effect of inclusion shape on the elastic moduli of a two-  
 586 phase material. *International Journal of solids and structures*, *2*(1), 1–8. doi:  
 587 [https://doi.org/10.1016/0020-7683\(66\)90002-3](https://doi.org/10.1016/0020-7683(66)90002-3)
- 588 Toksöz, M. N., Cheng, C., & Timur, A. (1976). Velocities of seismic waves in porous  
 589 rocks. *Geophysics*, *41*(4), 621–645. doi: <https://doi.org/10.1190/1.1440639>
- 590 Tsuji, T., & Iturrino, G. J. (2008). Velocity-porosity relationships in oceanic  
 591 basalt from eastern flank of the Juan de Fuca Ridge: The effect of crack  
 592 closure on seismic velocity. *Exploration Geophysics*, *39*(1), 41–51. doi:  
 593 <https://doi.org/10.1071/EG08001>
- 594 Vanorio, T., Prasad, M., & Nur, A. (2003). Elastic properties of dry clay mineral  
 595 aggregates, suspensions and sandstones. *Geophysical Journal International*,

- 596 155(1), 319–326. doi: <https://doi.org/10.1046/j.1365-246X.2003.02046.x>
- 597 Voigt, J. R., & Hamilton, C. W. (2018). Investigating the volcanic versus aqueous  
598 origin of the surficial deposits in Eastern Elysium Planitia, Mars. *Icarus*, 309,  
599 389–410. doi: <https://doi.org/10.1016/j.icarus.2018.03.009>
- 600 Waite, W. F., Santamarina, J. C., Cortes, D. D., Dugan, B., Espinoza, D., Ger-  
601 maine, J., . . . others (2009). Physical properties of hydrate-bearing sediments.  
602 *Reviews of geophysics*, 47(4). doi: <https://doi.org/10.1029/2008RG000279>
- 603 Wang, C.-y., Manga, M., & Wong, A. (2005). Floods on Mars released from ground-  
604 water by impact. *Icarus*, 175(2), 551–555. doi: <https://doi.org/10.1016/j>  
605 [.icarus.2004.12.003](https://doi.org/10.1016/j.icarus.2004.12.003)
- 606 Warner, N., Golombek, M., Ansan, V., Marteau, E., Williams, N., Grant, J., . . .  
607 others (2022). In Situ and Orbital Stratigraphic Characterization of the In-  
608 Sight Landing Site—A Type Example of a Regolith-Covered Lava Plain on  
609 Mars. *Journal of Geophysical Research: Planets*, 127(4), e2022JE007232. doi:  
610 <https://doi.org/10.1029/2022JE007232>
- 611 Weiss, D. K., & Head, J. W. (2017). Evidence for stabilization of the ice-  
612 cemented cryosphere in earlier Martian history: Implications for the current  
613 abundance of groundwater at depth on Mars. *Icarus*, 288, 120–147. doi:  
614 <https://doi.org/10.1016/j.icarus.2017.01.018>
- 615 Wernicke, L. J., & Jakosky, B. M. (2021). Martian hydrated minerals: A significant  
616 water sink. *Journal of Geophysical Research: Planets*, 126(3), e2019JE006351.  
617 doi: <https://doi.org/10.1029/2019JE006351>
- 618 Wieczorek, M. A., Broquet, A., McLennan, S. M., Rivoldini, A., Golombek, M., An-  
619 tonangeli, D., . . . others (2022). InSight constraints on the global character of  
620 the Martian crust. *Journal of Geophysical Research: Planets*, e2022JE007298.  
621 doi: <https://doi.org/10.1029/2022JE007298>
- 622 Woeber, A., Katz, S., & Ahrens, T. (1963). Elasticity of selected rocks and minerals.  
623 *Geophysics*, 28(4), 658–663. doi: <https://doi.org/10.1190/1.1439242>
- 624 Wright, V., Dasent, J., Kilburn, R., & Manga, M. (2022). A Minimally Ce-  
625 mented Shallow Crust Beneath InSight. *Geophysical Research Letters*, 49(15),  
626 e2022GL099250. doi: <https://doi.org/10.1029/2022GL099250>
- 627 Zong, J., Stewart, R. R., Dyaaur, N., & Myers, M. T. (2017). Elastic properties of  
628 rock salt: Laboratory measurements and Gulf of Mexico well-log analysis. *Geo-*  
629 *physics*, 82(5), D303–D317. doi: <https://doi.org/10.1190/geo2016-0527.1>

1 **Supporting Information for “Lithology, pore-filling**  
2 **media, and pore closure depth beneath InSight on**  
3 **Mars inferred from shear wave velocities”**

Richard Kilburn<sup>1</sup>, Jhardel Dasent<sup>1</sup>, Vashan Wright<sup>1</sup>, and Michael Manga<sup>2</sup>

4 <sup>1</sup>University of California San Diego, Scripps Institution of Oceanography, La Jolla, CA, 92037

5 <sup>2</sup>University of California Berkeley, Earth and Planetary Science Department, Berkeley, CA, 94709

6 **Contents of this file**

- 7 1. Method S1  
8 2. Figures S1 to S2  
9 3. Tables S1 to S2

---

Corresponding author: R. Kilburn, (rkilburn@ucsd.edu)

## 10 **Introduction**

11 This Supporting Information contains the equations for the rock physics models that  
12 we use, two supporting figures, and two supporting tables. The rock physics models that  
13 we use are the Hertz-Mindlin granular media model (Mindlin, 2021), the cementation  
14 model (Dvorkin & Nur, 1996), and the Berryman self-consistent fractured media model  
15 (Berryman, 1980). We refer interested readers to the papers cited above and Mavko,  
16 Mukerji, and Dvorkin (2020) for more detailed derivations and descriptions of each model.  
17 The figures in this Supplementary Information present results from the Berryman self-  
18 consistent fractured media model. Tables S1 and S2 in this Supplementary Information  
19 outline and describe the notation for the equations, symbols, and functions presented in  
20 this work.

21 **Method S1**

22 We use granular and fractured media rock physics models to calculate dry-frame elastic  
 23 moduli. We use the Hertz-Mindlin rock physics model (Mindlin, 2021) for cementless sed-  
 24 iments, the cementation model (Dvorkin & Nur, 1996) for cemented sediments (whether  
 25 the cements are at grain contacts or surrounding grains in contact), and the Berryman  
 26 self-consistent fractured media model (Berryman, 1980) for fractured rocks. The notations  
 27 for all the equations are in Table S2.

28 The equations for the Hertz-Mindlin rock physics model (Mindlin, 2021) are,

$$K_{HM} = \left[ \frac{C^2(1-\phi)^2\mu_m^2}{18\pi^2(1-\nu_m)^2} P \right]^{1/3}, \quad (1)$$

$$\mu_{HM} = \frac{2+3f-\nu_m(1+3f)}{5(2-\nu_m)} \left[ \frac{3C^2(1-\phi)^2\mu^2}{2\pi^2(1-\nu_m)^2} P \right]^{1/3}. \quad (2)$$

29 The equations for the cementation model (Dvorkin & Nur, 1996) are,

$$K_{CEM} = \frac{1}{6} C (1-\phi_c) M_c \hat{S}_n, \quad (3)$$

$$\mu_{CEM} = \frac{3}{5} K_{CEM} + \frac{3}{20} C (1-\phi_c) \mu_c \hat{S}_\tau, \quad (4)$$

$$M_c = \rho_c V_{Pc}^2, \quad (5)$$

$$\mu_c = \rho_c V_{Sc}^2 \quad (6)$$

$$\hat{S}_n = A_n \alpha_c^2 + B_n \alpha_c + C_n \quad (7)$$

$$A_n = -0.024153 \Lambda_n^{-1.3646}, \quad (8)$$

$$B_n = 0.20405 \Lambda_n^{-0.89008}, \quad (9)$$

$$C_n = 0.00024649 \Lambda_n^{-1.9864}, \quad (10)$$

$$\hat{S}_\tau = A_\tau \alpha_c^2 + B_\tau \alpha_c + C_\tau, \quad (11)$$

$$A_\tau = -10^{-2} (2.26v_g^2 + 2.07v_g + 2.3) \Lambda_\tau^{0.079v_g^2+0.1754v_g-1.342}, \quad (12)$$

$$B_\tau = (0.0573v_g^2 + 0.0937v_g + 0.202) \Lambda_\tau^{0.0274v_g^2+0.0529v_g-0.8765}, \quad (13)$$

$$C_\tau = 10^{-4} (9.654v_g^2 + 4.945v_g + 3.1) \Lambda_\tau^{0.01867v_g^2+0.4011v_g-1.8186}, \quad (14)$$

$$\Lambda_n = \frac{2\mu_c (1 - v_g) (1 - v_c)}{\pi\mu (1 - 2v_c)}, \quad (15)$$

$$\Lambda_\tau = \frac{\mu_c}{\pi\mu}, \quad (16)$$

$$\alpha_c = \frac{a}{R}. \quad (17)$$



30 The equations for the Berryman self-consistent fractured media model (Berryman, 1980)

31 are,

$$\sum_{i=1}^N x_i (K_i - K_{SC}^*) P^{*i} = 0, \quad (18)$$

$$\sum_{i=1}^N x_i (\mu_i - \mu_{SC}^*) Q^{*i} = 0, \quad (19)$$

$$P = \frac{1}{3} T_{iijj}, \quad (20)$$

$$Q = \frac{1}{5} (T_{ijij} - \frac{1}{3} T_{iijj}), \quad (21)$$

32 where  $T_{ijkl}$  is a strain tensor relating far-field and intra-ellipsoid strains given by Te Wu

33 (1966). The tensors  $T_{iijj}$  and  $T_{ijij}$  are given by,

$$T_{iijj} = \frac{3F_1}{F_2}, \quad (22)$$

$$T_{ijij} - \frac{1}{3} T_{iijj} = \frac{2}{F_3} + \frac{1}{F_4} + \frac{F_4 F_5 + F_6 F_7 - F_8 F_9}{F_2 F_4}, \quad (23)$$

34 where,

$$F_1 = 1 + A \left[ \frac{3}{2} (f_{sc} + \theta) - R \left( \frac{3}{2} f_{sc} + \frac{5}{2} \theta - \frac{4}{3} \right) \right], \quad (24)$$

$$F_2 = 1 + A \left[ 1 + \frac{3}{2} (f_{sc} + \theta) - \frac{1}{2} R (3f_{sc} + 5\theta) \right] + B(3 - 4R) + \frac{1}{2} A(A + 3B)(3 - 4R) [f_{sc} + \theta - R(f_{sc} - \theta + 2\theta^2)], \quad (25)$$

$$F_3 = 1 + A \left[ 1 - \left( f_{sc} + \frac{3}{2}\theta \right) + R(f_{sc} + \theta) \right], \quad (26)$$

$$F_4 = 1 + \frac{1}{4}A [f_{sc} + 3\theta - R(f_{sc} - \theta)], \quad (27)$$

$$F_5 = A \left[ -f_{sc} + R \left( f_{sc} + \theta - \frac{4}{3} \right) \right] + B\theta(3 - 4R), \quad (28)$$

$$F_6 = 1 + A[1 + f_{sc} - R(f_{sc} + \theta)] + B(1 - 0)(3 - 4R), \quad (29)$$

$$F_7 = 2 + \frac{1}{4}[3f_{sc} + 9\theta - R(3f_{sc} + 5\theta)] + B\theta(3 - 4R), \quad (30)$$

$$F_8 = A \left[ 1 - 2R + \frac{1}{2}f_{sc}(R - 1) + \frac{1}{2}\theta(5R - 3) \right] + B(1 - \theta)(3 - 4R), \quad (31)$$

$$F_9 = A [(R - 1)f_{sc} - R\theta] + B\theta(3 - 4R), \quad (32)$$

35 and the variables  $A$ ,  $B$ , and  $R$  are,

$$A = \mu_i/\mu_m - 1, \quad (33)$$

$$B = \frac{1}{3} \left( \frac{K_i}{K_m} - \frac{\mu_i}{\mu_m} \right), \quad (34)$$

$$R = \frac{(1 - 2v_m)}{2(1 - v_m)}. \quad (35)$$

<sup>36</sup>  $\theta$  and  $f_{sc}$  are functions given by,

$$\theta = \begin{cases} \frac{\alpha_{sc}}{(\alpha_{sc}^2 - 1)^{3/2}} \left[ \alpha_{sc} (\alpha_{sc}^2 - 1)^{1/2} - \cosh^{-1} \alpha_{sc} \right] \\ \frac{\alpha_{sc}}{(1 - \alpha_{sc}^2)^{3/2}} \left[ \cos^{-1} \alpha_{sc} - \alpha_{sc} (1 - \alpha_{sc}^2)^{1/2} \right], \end{cases} \quad (36)$$

for oblate spheroids ( $\alpha_{sc} < 1$ ),

$$f_{sc} = \frac{\alpha_{sc}^2}{1 - \alpha_{sc}^2} (3\theta - 2). \quad (37)$$

## References

- 37 Berryman, J. G. (1980). Long-wavelength propagation in composite elastic media I.  
38 Spherical Inclusions II. Ellipsoidal inclusions. *The Journal of the Acoustical Society*  
39 *of America*, *68*(6), 1820–1831. doi: <https://doi.org/10.1121/1.385172>
- 40 Dvorkin, J., & Nur, A. (1996). Elasticity of high-porosity sandstones: Theory for two  
41 North Sea data sets. *Geophysics*, *61*(5), 1363–1370. doi: [https://doi.org/10.1190/](https://doi.org/10.1190/1.1444059)  
42 [1.1444059](https://doi.org/10.1190/1.1444059)
- 43 Knapmeyer-Endrun, B., Panning, M. P., Bissig, F., Joshi, R., Khan, A., Kim, D., ...  
44 others (2021). Thickness and structure of the martian crust from InSight seismic  
45 data. *Science*, *373*(6553), 438–443. doi: <https://doi.org/10.1126/science.abf8966>
- 46 Mavko, G., Mukerji, T., & Dvorkin, J. (2020). *The rock physics handbook*. Cambridge  
47 university press. doi: <https://doi.org/10.1017/9781108333016>
- 48 Mindlin, R. D. (2021). Compliance of Elastic Bodies in Contact. *Journal of Applied*  
49 *Mechanics*, *16*(3), 259–268. doi: [10.1115/1.4009973](https://doi.org/10.1115/1.4009973)
- 50 Te Wu, T. (1966). The effect of inclusion shape on the elastic moduli of a two-phase  
51 material. *International Journal of solids and structures*, *2*(1), 1–8. doi: [https://](https://doi.org/10.1016/0020-7683(66)90002-3)  
52 [doi.org/10.1016/0020-7683\(66\)90002-3](https://doi.org/10.1016/0020-7683(66)90002-3)

## 53 Figures S1 to S2

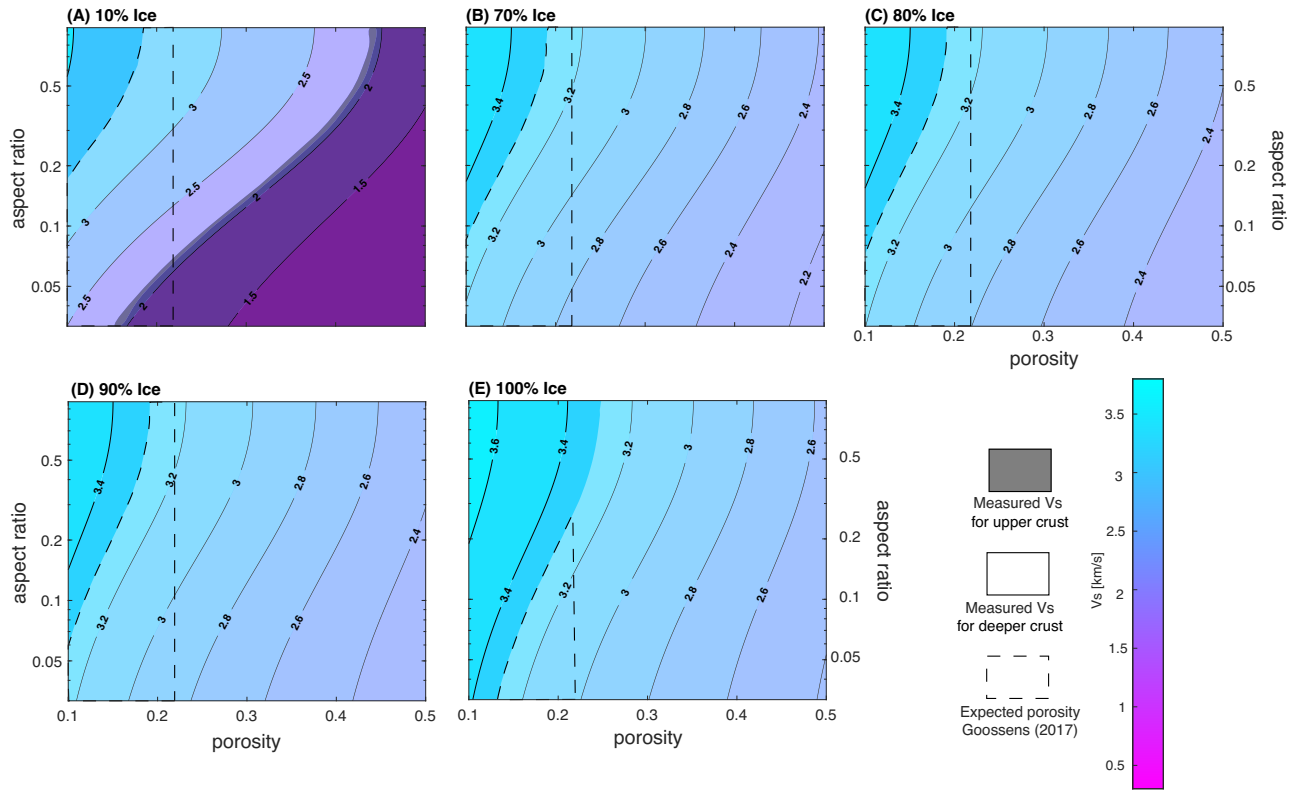


**Figure S1.** Rock physics templates showing relationships between  $V_s$ , aspect ratio  $\alpha$  (0.01 - 1.00), porosity  $\phi$  (0.1 - 0.5), and varying percentages of ice in the pores of a basalt host rock, either (A) 10%, (B) 70%, (C) 80%, (D) 90%, or (E) 100% ice. Y-axis is logarithmic.

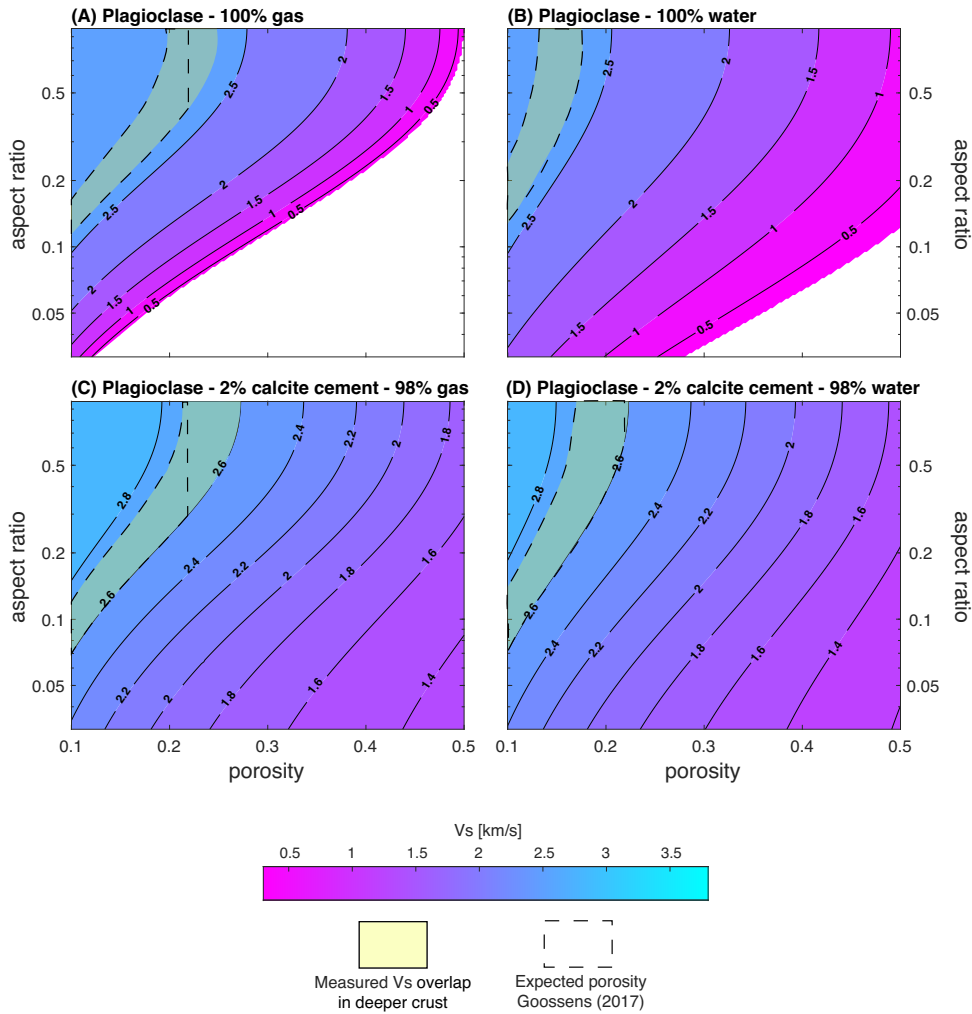


**Figure S2.** Rock physics templates showing relationships between  $V_s$ , aspect ratio  $\alpha$  (0.01 - 1.00), porosity  $\phi$  (0.1 - 0.5), and pore-filling media in a 100% plagioclase feldspar host rock. The yellow shading shows Knapmeyer-Endrun et al. (2021)'s measured  $V_s$  overlap range in the deeper crust (also see Figure ??). The pores are filled with either (A) gas, (B) water, (C) 2% calcite cement and 98% gas, or (D) 2% calcite cement and 98% water. Y-axis is logarithmic.

## 54 Tables S1 to S2

**Table S1.**  $P$  and  $Q$  coefficient equations for the background material ( $m$ ) and inclusions ( $i$ ).

Inclusion shape	$P^{mi}$	$Q^{mi}$
Spheres	$\frac{K_m + \frac{4}{3}\mu_m}{K_i + \frac{4}{3}\mu_m}$	$\frac{\mu_m + \zeta_m}{\mu_i + \zeta_m}$
Needles	$\frac{K_m + \mu_m + \frac{1}{3}\mu_i}{K_i + \mu_m + \frac{1}{3}\mu_i}$	$\frac{1}{5} \left( \frac{4\mu_m}{\mu_m + \mu_i} + 2\frac{\mu_m + \gamma_m}{\mu_i + \gamma_m} + \frac{K_i + \frac{4}{3}\mu_m}{K_i + \mu_m + \frac{1}{3}\mu_i} \right)$
Disks	$\frac{K_m + \frac{4}{3}\mu_i}{K_i + \frac{4}{3}\mu_i}$	$\frac{\mu_m + \zeta_i}{\mu_i + \zeta_i}$
Penny cracks	$\frac{K_m + \frac{4}{3}\mu_i}{K_i + \frac{4}{3}\mu_i + \pi\alpha\beta_m}$	$\frac{1}{5} \left[ 1 + \frac{8\mu_m}{4\mu_i + \pi\alpha(\mu_m + 2\beta_m)} + 2\frac{K_i + \frac{2}{3}(\mu_i + \mu_m)}{K_i + \frac{4}{3}\mu_i + \pi\alpha\beta} \right]$

$\beta = \mu \frac{3K + \mu}{3K + 4\mu}$ ,  $\gamma = \mu \frac{3K + \mu}{3K + 7\mu}$ ,  $\zeta = \frac{\mu}{6} \frac{9K + 8\mu}{K + 2\mu}$ ,  $\alpha =$  inclusion aspect ratio

**Table S2.** Notation for equations, variables, and formulas.

Symbol	Meaning
$K_{HM}$	Dry-frame bulk modulus from Hertz-Mindlin
$\mu_{HM}$	Dry-frame shear modulus from Hertz-Mindlin
$C$	Coordination number
$\phi$	Porosity
$\mu_m$	Mineral shear modulus
$\nu_m$	Mineral Poisson's ratio
$P$	Hydrostatic confining pressure
$f$	Volume fraction of rough versus smooth grains
$K_{CEM}$	Dry-frame bulk modulus from the cementation model
$\mu_{CEM}$	Dry-frame shear modulus from the cementation model
$\phi_c$	Critical porosity
$\mu_c$	shear modulus of the cement
$\hat{S}_n$	(proportional to) normal stiffness
$\hat{S}_\tau$	(proportional to) shear stiffness
$\rho_c$	Cement density
$V_{Pc}$	Cement P-wave velocity
$V_{Sc}$	Cement S-wave velocity
$\nu_c$	Cement Poisson's ratio
$\nu_g$	Mineral Poisson's ratio
$a$	Cement layer radius
$R$	Grain radius
$K_i$	Inclusion bulk modulus
$K_{SC}$	Self-consistent background medium effective bulk modulus
$\mu_i$	Inclusion shear modulus
$\mu_{SC}$	Self-consistent background medium effective shear modulus
$P, Q$	Geometric factors (Table S1)
$*i$	$i^{th}$ inclusion material
$x_i$	$i^{th}$ background material volume fraction
$N$	Number of phases
$T_{ijkl}$	Strain tensor (Te Wu, 1966)
$K_m$	Background material bulk modulus
$\mu_m$	Background material shear modulus
$\nu_m$	Background material Poisson's ratio
$\alpha_{sc}$	Aspect ratio
$\theta, f_{sc}$	Functions

(Note:  $f = 1$  means 100% rough grains)